Seasonal and Interannual Variabilities of the Central Indian Ocean Mode

LEI ZHOU

State Key Laboratory of Satellite Ocean Environment Dynamics, Second Institute of Oceanography, Hangzhou, and Institute of Oceanography, Shanghai Jiao Tong University, Shanghai, China

RAGHU MURTUGUDDE

University of Maryland, College Park, College Park, Maryland

DAKE CHEN

State Key Laboratory of Satellite Ocean Environment Dynamics, Second Institute of Oceanography, Hangzhou, China

YOUMIN TANG

State Key Laboratory of Satellite Ocean Environment Dynamics, Second Institute of Oceanography, Hangzhou, China, and Environmental Science and Engineering, University of Northern British Columbia, Prince George, British Columbia, Canada

(Manuscript received 19 August 2016, in final form 21 March 2017)

ABSTRACT

The central Indian Ocean (CIO) mode, an intrinsic coupled mode, plays an important role in the intraseasonal variabilities over the Indian monsoon region. Besides the intraseasonal variabilities, the CIO mode also has pronounced seasonal and interannual variabilities. The CIO mode is active during boreal summer but suppressed during boreal winter. The seasonality is mainly attributable to the barotropic instability, which is caused by the large meridional shear of zonal winds. By decomposing the temporal tendency of the meridional gradient of zonal winds, it is found that the zonal wind shear mainly follows the variation of the horizontal eddy flux, which indicates the importance of the multiscale interaction in tropical dynamics. The interannual variability of the CIO mode also depends on the energy transfer associated with the barotropic instability. The influences of El Niño or La Niña and Indian Ocean dipole–zonal mode (IODZM) on the CIO mode are analyzed. El Niño and La Niña have moderate impacts on the CIO mode. El Niño weakens the CIO mode and La Niña strengthens it via the changes in the low-level zonal wind shear. IODZM does not significantly change the amplitude of the CIO mode but can shift its latitudinal position by modifying the meridional shear of the zonal winds. The low-frequency variabilities of the CIO mode at seasonal and interannual time scales unveil the impacts of the background circulations at the intraseasonal variabilities during the Indian summer monsoon in a multiscale framework. While the low-frequency variabilities of this mode will clearly have an implication for monsoon variability and prediction, further studies are needed to quantify the impacts.

1. Introduction

The summer monsoon is the wet season of the Indian subcontinent and is the lifeline for billions of people living on the rim of the Indian Ocean. Intraseasonal variability, which is commonly known as the monsoon intraseasonal oscillation (MISO), is pronounced during the Indian summer monsoon (Goswami 2005; Shukla 2014). Many studies have confirmed that MISO stems from the tropical Indian Ocean, as a result of the northward-propagating intraseasonal variabilities. Yasunari (1980) was one of the pioneers, and comprehensive descriptions of MISO were given by Annamalai and Slingo (2001), Goswami (2005), and Waliser (2006). Several processes and mechanisms have been identified to be important for the northward-propagating intraseasonal variabilities, such as the surface heat flux (Webster 1983), the interaction between the perturbations and the background easterly wind shear (Jiang et al. 2004), the eddy-mediated regime transitions (Bordoni and Schneider 2008), the convective momentum transport (CMT; Kang et al. 2010), and the ocean–atmosphere

Corresponding author: Lei Zhou, lzhou@sio.org.cn

DOI: 10.1175/JCLI-D-16-0616.1

interactions (Yano and McBride 1998; Kemball-Cook and Wang 2001; Fu and Wang 2004; Zhou and Murtugudde 2014; Xi et al. 2015). Recently, a central Indian Ocean (CIO) mode was proposed in Zhou et al. (2017) as an intrinsic coupled mode that can explain the intraseasonal variabilities in the Indian monsoon. The CIO mode is represented by the covariability of intraseasonal sea surface temperature (SST) anomalies and intraseasonal low-level wind anomalies over the central Indian Ocean, and it captures the mechanistic links between the dynamic and thermodynamic fields. The CIO mode acts like a T junction and plays a role in the transition between the eastward-propagating intraseasonal variabilities (commonly known as the Madden–Julian oscillation) and the northward-propagating MISO. As a result, a high correlation between the CIO mode and the intraseasonal precipitation over the Bay of Bengal in boreal summer is found. The CIO mode and related processes have been diagnosed in Zhou et al. (2017) at intraseasonal time scales. As can be expected of this multiscale system, the CIO mode also has distinct features at seasonal–interannual time scales. Such low-frequency variability of the CIO mode and the driving mechanism are analyzed in this study. Decadal and multidecadal time scales and trends under global climate change will be diagnosed in a separate study especially in the context of the negative trend in the Indian summer monsoon and the erroneous representation of this trend in CMIP5 models (Saha et al. 2014; Roxy et al. 2015; Sabeerali et al. 2015).

At interannual time scales, El Niño–Southern Oscillation (ENSO) and the Indian Ocean dipole–zonal mode (IODZM) dominate over the Indo-Pacific region although some recent studies have posited that the tropical Atlantic can also influence the Indian monsoon variability (Pottapinjara et al. 2014, 2016). The long-term variability of the Indian summer monsoon is influenced by ENSO and IODZM. A negative correlation was found between ENSO and the Indian summer monsoon (Webster and Palmer 1997; Krishnamurthy and Kirtman 2003), but the relation appears to be nonstationary at decadal time scales (Kumar et al. 1999; Krishnamurthy and Goswami 2000). Especially in recent decades, the relation between ENSO and the Indian summer monsoon has weakened because of the influence of IODZM (Slingo and Annamalai 2000; Ashok et al. 2001; Sarkar et al. 2004), but the debate over the decadal shifts in Indian summer monsoon onset, withdrawal, and length of the rainy season continues (Sabeerali et al. 2014; Sahana et al. 2015). During the positive IODZM phase, warm SST anomalies over the western tropical Indian Ocean lead to anomalous updraft and surplus rainfall, compensating the El Niño–induced rainfall deficit over the monsoon region (Ashok et al. 2004). The relations between the Indian summer monsoon, ENSO, and IODZM extracted from observations and reanalysis products are confirmed by both theoretical and modeling studies (e.g., Li et al. 2003; Lau and Nath 2004). Because of the tangled interactions between the Indian and the Pacific Oceans, an appropriate combination of ENSO and IODZM is likely to have a better representation of the slow variability of Indian summer monsoon (Gadgil et al. 2004; also see Chen 2011; Lian et al. 2014) and may also need to consider the Atlantic zonal mode. By analogy, it is natural to expect that the interannual variability of the CIO mode is possibly influenced by both ENSO and IODZM as well. This is indeed the case and we report the detailed processes in this study. Any potential Atlantic influences on the CIO are not considered here.

For the rest of this paper, the data and methods are introduced in section 2. The seasonal and interannual variabilities as well as the dynamics are discussed in sections 3 and 4, respectively. The conclusions and discussion are presented in section 5.

2. Data and methods

Atmospheric variables, such as wind and precipitation for 1982–2014, are obtained from the daily National Centers for Environmental Prediction (NCEP)–National Center for Atmospheric Research (NCAR) reanalysis (Kalnay et al. 1996). The atmospheric variables are also obtained from daily ERA-Interim data, the global atmospheric reanalysis produced by the European Centre for Medium-Range Weather Forecasts (ECMWF; Uppala et al. 2005) for ensuring the robustness of our findings. SST data for 1982–2014 are obtained from the ¼° daily NOAA Optimum Interpolation SST (Reynolds et al. 2007), and the outgoing longwave radiation (OLR) data are available for 1982–2013 from the NOAA satellite data (Liebmann and Smith 1996). All intraseasonal variabilities are obtained with a 20–100-day-bandpass Butterworth filter.

The index for the CIO mode is the principal component (PC) of the first combined empirical orthogonal function (EOF) mode of the daily intraseasonal SST and daily intraseasonal zonal winds at 850 hPa, as described in Zhou et al. (2017). The domain for the EOF analysis is over the whole Indian Ocean, covering 20°N–20°S, 40°–120°E. Each field is normalized by subtracting its regional mean and then dividing by its regional variance within the above domain before doing the EOF analysis, so that the SST and winds become dimensionless and are comparable in magnitude. The CIO mode index (CI) is shown in Fig. 1a with a blue curve. Although CI mainly captures the intraseasonal variabilities, there are also clear low-frequency variabilities in CI. To highlight the

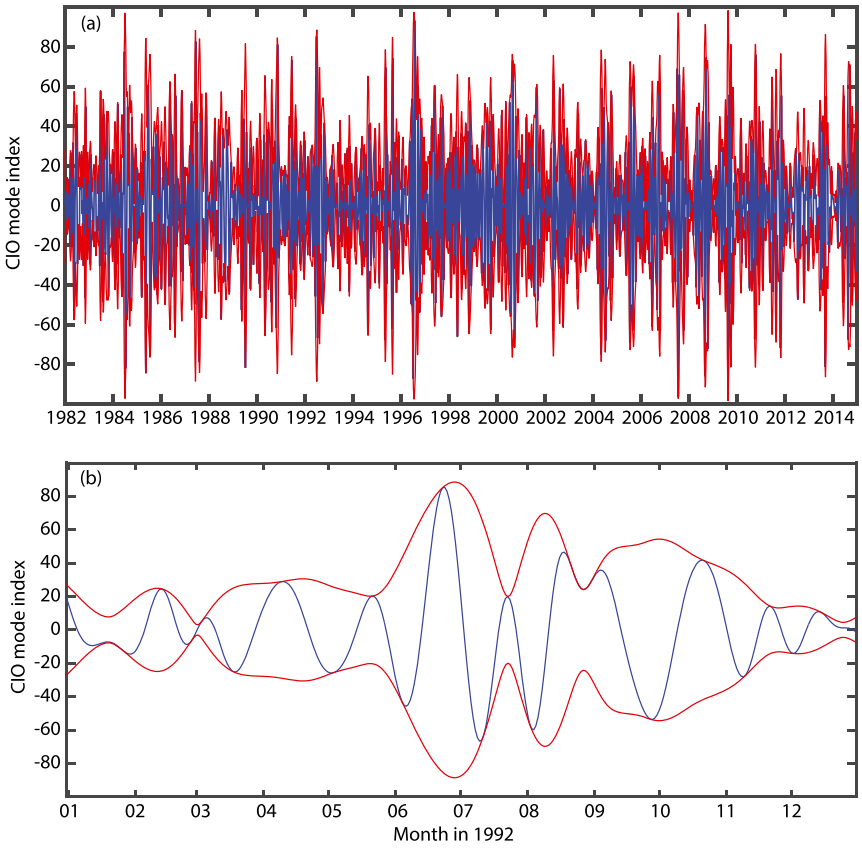

FIG. 1. (a) The CI (blue line; i.e., the PC of the first combined EOF mode) and its envelope (EI; red lines) obtained with the Hilbert transform. The top red line denotes positive EI and the bottom red line denotes negative EI. (b) Zoom in of (a) for the randomly selected year of 1992.

latter, the envelope of CI (EI) is computed using the Hilbert transform; that is, $EI = |\mathcal{H}(CI)|$, where $\mathcal{H}$ denotes the Hilbert transform (red curves in Fig. 1a). The Hilbert transform is a common way to detect the envelope of a signal, which has been used to extract the low-frequency variabilities in both the ocean and the atmosphere (e.g., Longuet-Higgins 1984; Ouergli 2002). To show the effect of the envelope clearly, a zoom-in time series of CI and EI are shown in Fig. 1b for a randomly selected year of 1992. The following analyses mainly rely on the seasonal and interannual variabilities of EI.

In the following analysis, a two-sample Student's t test, assuming that the two samples have unknown and unequal variances, is applied to test the statistical significance of the differences between two groups at a 95% confidence level.

3. Seasonal variability of the CIO mode

The climatological seasonal variability (daily data averaged from 1982 to 2014) of EI is shown in Fig. 2. It is obvious that the CIO mode is active during Indian summer monsoon from June to September but suppressed during boreal winter from December to March. Note that large (small) EI in Fig. 2 does not indicate a positive (negative) phase of the CIO mode. Instead, large (small) EI indicates that the amplitudes of the CIO mode for both the positive and the negative phases are enhanced (suppressed) during boreal summer (winter). In other words, the background state is favorable (unfavorable) for the CIO mode during boreal summer (winter). Thus, the question that will be addressed in this study is—what in the background state facilitates energizing the CIO mode during the Indian summer monsoon? Another distinct feature of the seasonal variation of EI in Fig. 2 is the dip in EI from early May to early June, which, however, is not likely to be attributable to the monsoon break periods or the "bogus" monsoon onset. Figure 2 shows the climatological seasonal variation of EI. While the break spells (Krishnan et al. 2000; Rajeevan et al. 2010) and the bogus onset of monsoon (Fasullo and Webster 2003) are both intraseasonal

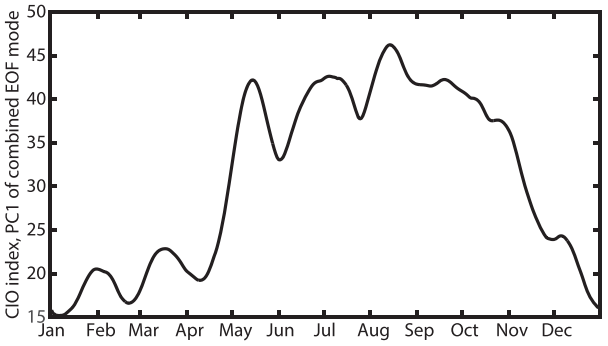

FIG. 2. The climatological seasonal variation of EI, which is the mean daily index from 1982 to 2014.

features, they are largely removed in the climatological mean. (The possible reason for the dip is discussed later using Fig. 7.)

Since the CIO mode is composed of the anomalies of low-level winds, the variabilities of the CIO mode can be detected from the variation of intraseasonal atmospheric kinetic energy (KE′; the intraseasonal variability of a variable is denoted with a prime hereafter). Following Zhou et al. (2012), the kinetic energy budget at the intraseasonal time scale in isobaric coordinates can be decomposed as

$$\frac{\partial \mathrm{KE}'}{\partial t} = -\overline{\mathbf{u}} \cdot \nabla \mathrm{KE}' + [\mathrm{KE}' \times \mathrm{KE}''] + [\mathrm{KE}' \times \overline{\mathrm{KE}}] - \nabla \cdot (\mathbf{u}'\Phi') + [\mathrm{KE}' \times \mathrm{PE}'] + \mathrm{EV} + R, \quad (1)$$

where $\mathbf{u} = u\mathbf{i} + v\mathbf{j} + \omega\mathbf{k}$ is the three-dimensional velocity in isobaric coordinates ($\omega = dp/dt$), Φ is the geopotential, and $\nabla = \mathbf{i}\partial/\partial x + \mathbf{j}\partial/\partial y + \mathbf{k}\partial/\partial p$. Following the definition in Zhou et al. (2012) and Holton and Hakim (2013), $[\mathrm{KE}' \times \mathrm{KE}'']$ denotes the energy conversion between kinetic energy of the intraseasonal variabilities and the kinetic energy of the mesoscale variabilities, $[\mathrm{KE}' \times \overline{\mathrm{KE}}]$ represents the kinetic energy exchange between the intraseasonal variabilities and the background state, $[\mathrm{KE}' \times \mathrm{PE}']$ captures the energy transfer between the kinetic energy and the potential energy of the intraseasonal variabilities, the EV term is the dot product of the velocity and the eddy momentum flux at the intraseasonal time scale [see Zhou et al. (2012) for more details], and R is the residual term. During the Indian summer monsoon from June to September, KE′ is shown in Fig. 3a. It is pronounced in three regions over the Indian Ocean. One is from 75° to 95°E straddling the equator, which is exactly the region of the CIO mode. The other two regions are the Arabian Sea and the Bay of Bengal, which are to the west of the heavy monsoonal precipitation in the two regional oceans (not shown). The high KE′ in these two regions are understandable and important for the Indian summer monsoon, but they are not directly related to the CIO mode. Thus, they are not the focus for the following discussion. During boreal winter from December to March, KE′ over the central Indian Ocean is relatively small, and a pronounced KE′ occurs along 10°S, being roughly

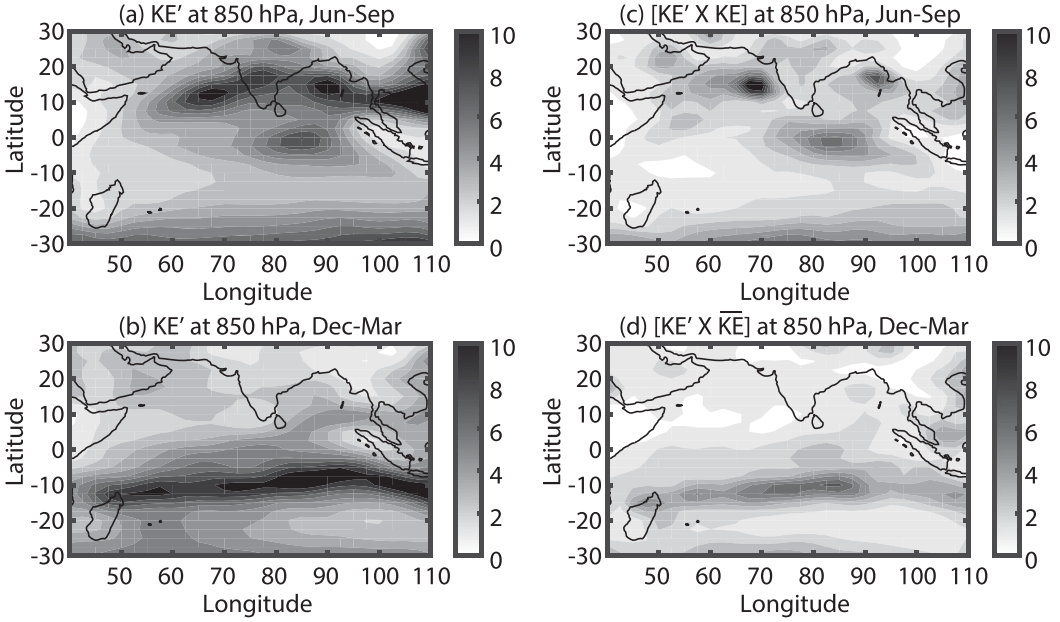

FIG. 3. (a) KE′ at 850 hPa (J kg^{-1}) averaged over boreal summer from June to September. (b) As in (a), but averaged over boreal winter from December to March. (c),(d) As in (a),(b), but for $[\mathrm{KE}' \times \overline{\mathrm{KE}}]$ (J day^{-1} kg^{-1}).

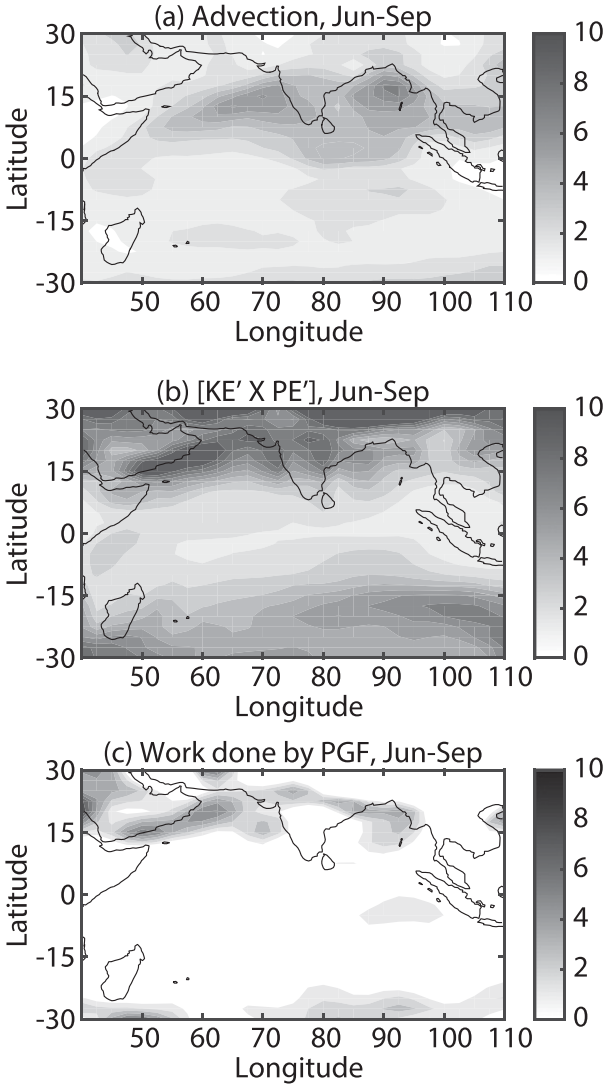

FIG. 4. Terms of the kinetic energy budget in Eq. (1) at 850 hPa (J day^{-1} kg^{-1}) averaged over boreal summer from June to September for (a) the horizontal advection, (b) [KE′ × PE′], and (c) the work done by the pressure gradient force.

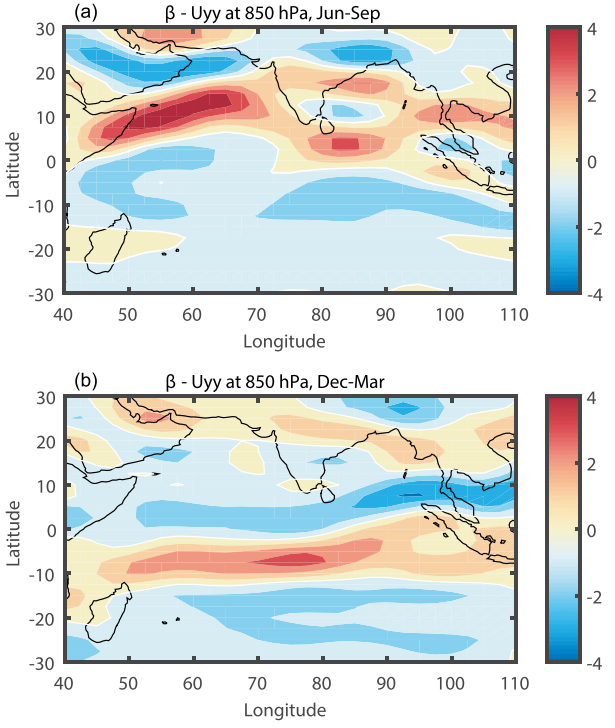

FIG. 5. Meridional gradient of QGPV at 850 hPa (10^{-11} m^{-1} s^{-1}) for the (a) Indian summer monsoon (from June to September) and (b) boreal winter (from December to March).

consistent with the ITCZ in the Southern Hemisphere (Fig. 3b). Each term in Eq. (1) is examined individually. It turns out that only [KE′ × $\overline{\text{KE}}$] shows a similar pattern to that of KE′ in both boreal summer and boreal winter, as shown in Figs. 3c and 3d, respectively. The advection term in the KE′ budget (Fig. 4a) is large in the Bay of Bengal and the Arabian Sea but is moderate over the tropical Indian Ocean. The [KE′ × PE′] is pronounced in the subtropics (Fig. 4b) but is small over the equatorial region. The work done by the pressure gradient force in Eq. (1) is generally small, as shown in Fig. 4c. The [KE′ × KE″] is much smaller than other terms, so it is not shown. Usually, the energy transfer from the mean kinetic energy to the kinetic energy of intraseasonal variabilities is caused by the barotropic instability of the background state (Vallis 2006; Holton and Hakim 2013). In addition, a meridionally tilted structure can be seen in the vertical profiles of zonal winds (not shown), which helps to carry the zonal momentum during the barotropic energy conversion.

It is well known that the necessary condition for barotropic instability is that the meridional gradient of quasigeostrophic potential vorticity (QGPV; $dq/dy = \beta - \partial^2 U/\partial y^2$, where q is QGPV, β is the meridional gradient of the Coriolis parameter, and U is the background zonal velocity) changes sign within the study region (Vallis 2006). Figure 5 shows dq/dy in the lower troposphere at 850 hPa during the Indian summer monsoon and during boreal winter. During the Indian summer monsoon, positive and negative values occur alternatively in the meridional direction from about 10°S to the northern Bay of Bengal (~20°N), which is indicative of the necessary condition for the barotropic instability being satisfied. On the contrary, dq/dy during boreal winter is mostly negative, and the necessary condition for barotropic instability in the Northern Hemisphere does not occur. However, in the Southern Hemisphere, the zonal belt of a negative–positive–negative pattern of dq/dy can satisfy the

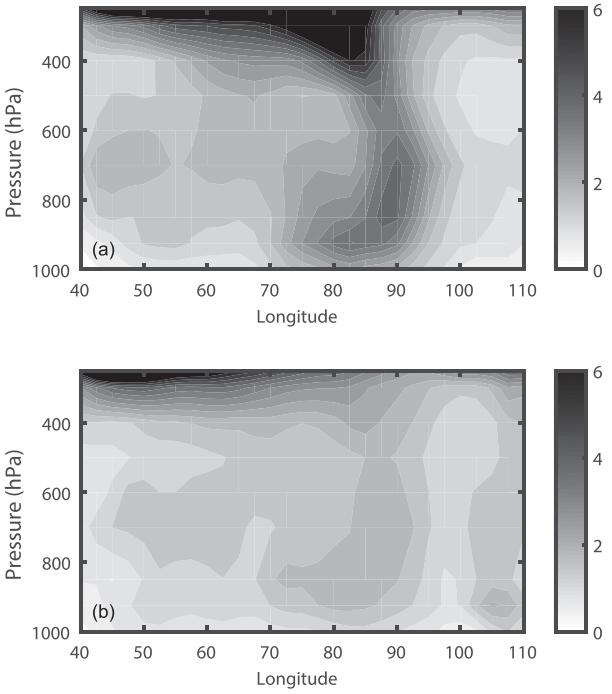

FIG. 6. Vertical profile of the mean $[\mathrm{KE}' \times \overline{\mathrm{KE}}]$ ($\mathrm{J\,day^{-1}\,kg^{-1}}$) averaged between 5°N and 5°S (a) during Indian summer monsoon (from June to September) and (b) during boreal winter (from December to March).

necessary condition for barotropic instability and lead to large $[\mathrm{KE}' \times \overline{\mathrm{KE}}]$ along 10°S, which is consistent with the energy conversion shown in Fig. 3d. According to the analytical results of the barotropic instability of edge waves (Vallis 2006), the zonal scale of the barotropic instability is approximately $0.63/a$, where a is half of the meridional scale of zonal winds. In the current situation, a is about 15° latitude (half distance from 10°S to 20°N; Fig. 5a). Hence, the zonal scale of barotropic instability is about 23° longitude, which is consistent with the zonal scale of the CIO mode (roughly from 75° to 95°E) and is also consistent with the length scale of the monsoon trough, which is usually 2000–3000 km. Obviously, there are distinct differences between the highly simplified model and the real situation. But the estimate based on the idealized edge waves qualitatively supports the relation between the barotropic instability and the low-frequency variabilities of the CIO mode.

The vertical profiles of $[\mathrm{KE}' \times \overline{\mathrm{KE}}]$ in the tropics and their differences are shown in Fig. 6. It confirms that the energy transfer due to barotropic instability is pronounced between 75° and 95°E during Indian summer monsoon and it is significantly larger than the counterpart in boreal winter. In addition, pronounced $[\mathrm{KE}' \times \overline{\mathrm{KE}}]$ over the central Indian Ocean during the Indian summer monsoon is uniform through the whole air column, which is consistent with the nearly barotropic structure of the CIO mode (Zhou et al. 2017).

For barotropic instability, the meridional shear and the tendency of the background zonal wind are the key. In isobaric coordinates, the zonal momentum equation at an isobaric level is written as

$$\frac{Du}{Dt} - (f + \beta y)v = -\frac{\partial \Phi}{\partial x} + X, \tag{2}$$

where f is the Coriolis parameter, $D/Dt = \partial/\partial t + u\partial/\partial x + v\partial/\partial y + \omega\partial/\partial p$, and X denotes the residual and unresolved terms. Taking the zonal mean within a domain (e.g., over the Indian Ocean), one has (see the appendix for details)

$$\begin{aligned}\frac{\overline{D}}{Dt}\overline{u} - (f + \beta y)\overline{v} &= \left(\frac{\partial}{\partial t} + \overline{v}\frac{\partial}{\partial y} + \overline{\omega}\frac{\partial}{\partial p}\right)\overline{u} - (f + \beta y)\overline{v} \\ &= -\frac{\partial \overline{u'v'}}{\partial y} - \frac{\partial \overline{u'\omega'}}{\partial p} - \frac{\overline{u}\Delta u' + \Delta(u'u') + \Delta\Phi'}{L} + \overline{X}, \end{aligned} \tag{3}$$

where the overbar denotes the zonal mean (e.g., $\overline{u} = L^{-1}\int_{X_W}^{X_E} u\,dx$), X_E and X_W denote locations of eastern and western boundaries, respectively, and $L = X_E - X_W$ is the zonal length of the domain. Then, taking the y derivative of Eq. (3), one has the tendency equation for $\partial\overline{u}/\partial y$:

$$\frac{\partial}{\partial t}\left(\frac{\partial \overline{u}}{\partial y}\right) = \mathrm{ADV} + \beta_{\mathrm{term}} + H_{\mathrm{eddy}} + V_{\mathrm{eddy}} + \mathrm{BRY} + \frac{\partial \overline{X}}{\partial y}, \tag{4}$$

where

$$\mathrm{ADV} = -\frac{\partial \overline{v}}{\partial y}\frac{\partial \overline{u}}{\partial y} - \overline{v}\frac{\partial^2 \overline{u}}{\partial y^2} - \frac{\partial \overline{\omega}}{\partial y}\frac{\partial \overline{u}}{\partial p} - \overline{\omega}\frac{\partial^2 \overline{u}}{\partial y \partial p}$$

represents the influence of advection, $\beta_{\mathrm{term}} = -(f + \beta y)\partial\overline{v}/\partial y - \beta\overline{v}$ represents the influence of Earth's rotation, $H_{\mathrm{eddy}} = -\partial^2(\overline{u'v'})/\partial y^2$ represents the horizontal eddy flux, $V_{\mathrm{eddy}} = -\partial^2(\overline{u'w'})/\partial y \partial p$ represents the vertical eddy flux, $\mathrm{BRY} = -\partial/\partial y[\Delta(uu' + \Phi')/L]$ represents the influences from the two boundaries, and $\partial\overline{X}/\partial y$ denotes the net influence of the residual terms, which likely represent unresolved eddy processes.

The seasonal variabilities of $\partial\overline{u}/\partial y$ and $\partial/\partial t(\partial\overline{u}/\partial y)$ at 850 hPa averaged over the Indian Ocean from 40° to 120°E are shown in Fig. 7. The zonal averages over the central Indian Ocean domain (e.g., from 75° to 95°E) are essentially similar to Fig. 7, so they are not shown explicitly. The meridional gradient of zonal mean zonal velocity begins to increase in March (color shading in

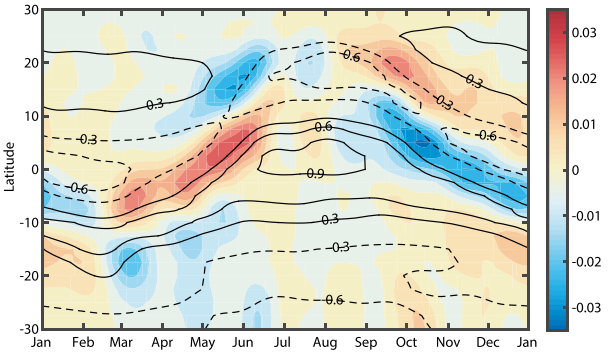

FIG. 7. Daily mean $\partial\overline{u}/\partial y$ (contours; day^{-1}) and $\partial/\partial t(\partial\overline{u}/\partial y)$ (color shading; day^{-2}) averaged from 1982 to 2014 at 850 hPa over the Indian Ocean from 40° to 120°E.

Fig. 7). Along with the northward migration of the sun and ITCZ, positive $\partial/\partial t(\partial\overline{u}/\partial y)$ also moves northward until June. In March, positive $\partial\overline{u}/\partial y$ exists along 10°S (solid contours in Fig. 7). As a result of positive $\partial/\partial t(\partial\overline{u}/\partial y)$ and the northward migration, positive $\partial\overline{u}/\partial y$ increases and also moves northward. However, since $\partial/\partial t(\partial\overline{u}/\partial y)$ in the Southern Hemisphere during boreal summer is small, $\partial\overline{u}/\partial y$ remains positive along 10°S. Thus, the belt of positive $\partial\overline{u}/\partial y$ during boreal summer actually expands. In May, to the north of positive $\partial\overline{u}/\partial y$, negative $\partial/\partial t(\partial\overline{u}/\partial y)$ appears, and $\partial\overline{u}/\partial y$ becomes more negative. Because of the strong positive tendency of $\partial\overline{u}/\partial y$ between the equator and 10°N, negative $\partial\overline{u}/\partial y$ reduces and almost disappears from early May to early June, which corresponds to the dip in the seasonal EI shown in Fig. 2. After early June, the negative $\partial/\partial t(\partial\overline{u}/\partial y)$ reinforces the negative $\partial\overline{u}/\partial y$. The pattern of an alternative positive $\partial\overline{u}/\partial y$ and negative $\partial\overline{u}/\partial y$ in the meridional direction is favorable for the barotropic instability. As a result, EI rebounds from the dip after early June as shown in Fig. 2. During the Indian summer monsoon from June to September, both positive $\partial/\partial t(\partial\overline{u}/\partial y)$ from the equator to 10°N and negative $\partial/\partial t(\partial\overline{u}/\partial y)$ from 10° to 20°N become small. As a result, positive $\partial\overline{u}/\partial y$ reaches a maximum along the equator, and negative $\partial\overline{u}/\partial y$ reaches a minimum to the north. Thus, the meridional gradient of relative vorticity $\partial^2\overline{u}/\partial y^2$ becomes large enough to overcome the meridional gradient of planetary vorticity β, and the necessary condition for the barotropic instability can be satisfied (Fig. 5a). In October, $\partial/\partial t(\partial\overline{u}/\partial y)$ turns negative and retreats southward along with the ITCZ. Correspondingly, $\partial\overline{u}/\partial y$ decreases in the Northern Hemisphere. But, since $\partial/\partial t(\partial\overline{u}/\partial y)$ is still moderate in the Southern Hemisphere, $\partial\overline{u}/\partial y$ does not change much either. and the belt for positive $\partial\overline{u}/\partial y$ shrinks. The reduction of $\partial\overline{u}/\partial y$ shuts down the barotropic instability and suppresses the CIO mode.

The components for $\partial/\partial t(\partial\overline{u}/\partial y)$ in Eq. (4) along 5°N, where $\partial/\partial t(\partial\overline{u}/\partial y)$ reaches its maximum and minimum, are shown in Fig. 8. The variation of $\partial/\partial t(\partial\overline{u}/\partial y)$ is small (black line) and not clearly visible in Fig. 8a but is discernible in Fig. 8b. Along 5°N, $\partial\overline{u}/\partial y$ begins to increase from May and lasts until June. During the Indian summer monsoon from late June to September, $\partial/\partial t(\partial\overline{u}/\partial y)$ is close to zero, and hence $\partial\overline{u}/\partial y$ reaches a maximum, which is consistent with what is shown in Fig. 7. In Fig. 8a, during the Indian summer monsoon, one can see that advection (red curve) and β effect (blue curve) are two dominant terms, but they tend to cancel each other from May to September. In May, the sum of advection and the β effect contribute significantly to the positive $\partial/\partial t(\partial\overline{u}/\partial y)$ (red curve in Fig. 8b). But, from June to September, the sum of advection and the β effect are small or slightly negative. The variation of $\partial/\partial t(\partial\overline{u}/\partial y)$ mainly follows the horizontal eddy flux (cyan curve). The vertical eddy flux (yellow curve) is generally negligible, except from May to July when it cancels part of the horizontal eddy flux. The residual term is relatively small during the Indian summer monsoon, except from May to July, which indicates a relatively high reliability of the decomposition of $\partial/\partial t(\partial\overline{u}/\partial y)$. During boreal winter, the advection and β effect are very large, but they are offset by the unresolved processes, which are grouped into the residual term. As a result, the net tendency of $\partial\overline{u}/\partial y$ is quite small in the Northern Hemisphere. Since we intend to focus on the Indian summer monsoon, what specific processes may be involved in the unresolved term during boreal winter are not explored in this study. Overall, it can be concluded that for the meridional gradient of the background zonal wind during boreal summer, the horizontal advection and β term are two dominant components but they largely cancel each other. The variation of $\partial\overline{u}/\partial y$ is mainly controlled by the horizontal eddy flux.

4. Interannual variability of the CIO mode

Besides the seasonal variability, the CIO mode (EI) also has a pronounced interannual variability, as shown in Fig. 9 (solid line). The mean $[\mathrm{KE}' \times \overline{\mathrm{KE}}]$ at 850 hPa averaged during the Indian summer monsoon over the central Indian Ocean in each year are superimposed in Fig. 9 with a dashed line. The correlation coefficient between the interannual EI and the interannual barotropic energy transfer is 0.69, which is statistically significant at a 95% confidence level. The high correlation indicates again that the barotropic instability is the direct energy source for the CIO mode. In addition, both EI and barotropic energy conversion are coherent with the Indian summer monsoon. Note that EI represents

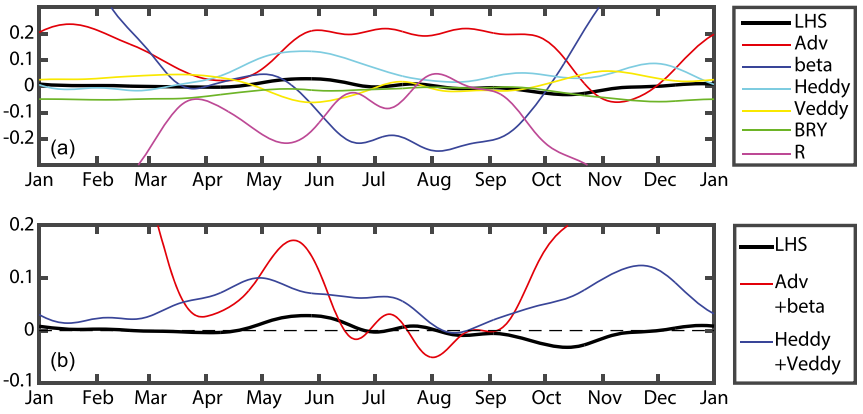

FIG. 8. (a) All terms (day^{-2}) in Eq. (4) along 5°N and (b) the three major components (day^{-2}) in Eq. (4): LHS denotes the $\partial/\partial t(\partial\overline{u}/\partial y)$ on the left-hand side of Eq. (4), Adv is the advection term, beta is the β_{term}, and R is the residual term. The domain for the zonal mean is the Indian Ocean basin from 40° to 120°E.

the low-frequency variability of the CIO mode, which mainly captures the intraseasonal variabilities (Fig. 1). Thus, EI is different from the seasonal variation of the Indian monsoon. In fact, there is a weak negative correlation between the seasonal and the intraseasonal monsoon variabilities, which implies that the Indian monsoon may be subject to different mechanisms at two different time scales. The seasonal evolution of the Indian monsoon was found to have a connection with the meridional gradient of temperature and baroclinic processes (e.g., Charney and Stern 1962), but this does not imply any contradiction with the above results. During the Indian summer monsoon, the heat-releasing center moves from the tropical Indian Ocean to the subtropics (Wu and Zhang 1998; Zhou and Murtugudde 2014), which leads to warming in the subtropics. Such a feature is captured by the daily tropospheric temperature gradient (TT) index (Goswami and Xavier 2005), which is the difference of the vertical mean temperature between 700 and 300 hPa averaged between a northern box (35°–10°N, 30°–110°E) and a southern box (10°N–15°S, 30°–110°E). The dash–dotted line in Fig. 9 shows the average of the envelope of the intraseasonal TT index in the northern box (the subtropical region) in each year. The correlation coefficient between the CIO index (solid line) and the Indian monsoon index (dash–dotted line) is 0.61, which is significant at the 95% confidence level [the influence of the bandpass filtering on the significance test of the correlation coefficient is removed following Bretherton et al. (1999)]. In contrast, the correlations between the interannual ENSO index (such as the Niño-3.4 index) or the IODZM index (such as the IOD index) and the TT index are insignificant (not shown), which is consistent with current understanding that the impacts of ENSO and IODZM on the Indian summer monsoon are not stable and have a large variance (Ashok et al. 2001; Krishnamurthy and Kirtman 2003; Sabeerali et al. 2014). The correlation between the MISO and the high-frequency intraseasonal variabilities (or commonly known as the quasi-biweekly oscillation) is insignificant in the region used for Fig. 9 (not shown). Moreover, Karmakar et al. (2015) showed that, at interannual time scales, the seasonal mean rainfall has an out-of-phase relation with the MISO but an in-phase relation with the high-frequency intraseasonal variabilities. Therefore, in the multiscale framework for the Indian monsoon, the components at different time scales have different interactive relations. The close relation between the CIO mode and the Indian summer monsoon at interannual time scale indicates the importance of the CIO mode

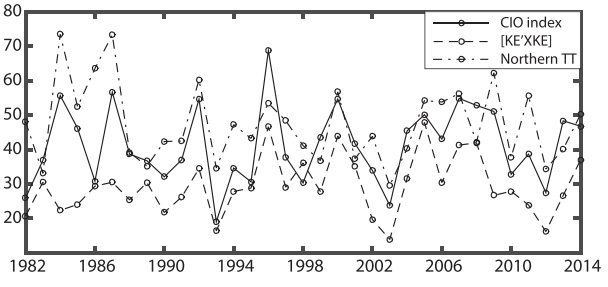

FIG. 9. EI averaged from June to September in each year (solid line). Mean [KE′ × $\overline{\text{KE}}$] at 850 hPa (10^{-1} J day^{-1} kg^{-1}), averaged over 5°–15°N, 75°–85°E, and also averaged from June to September in each year (dashed line). The envelope (obtained with the Hilbert transform) of intraseasonal TT index (0.01°C) in the northern box 35°–10°N, 30°–110°E averaged from June to September in each year (dash–dotted line). Note that the envelope of TT index is different from the seasonal variability of TT index.

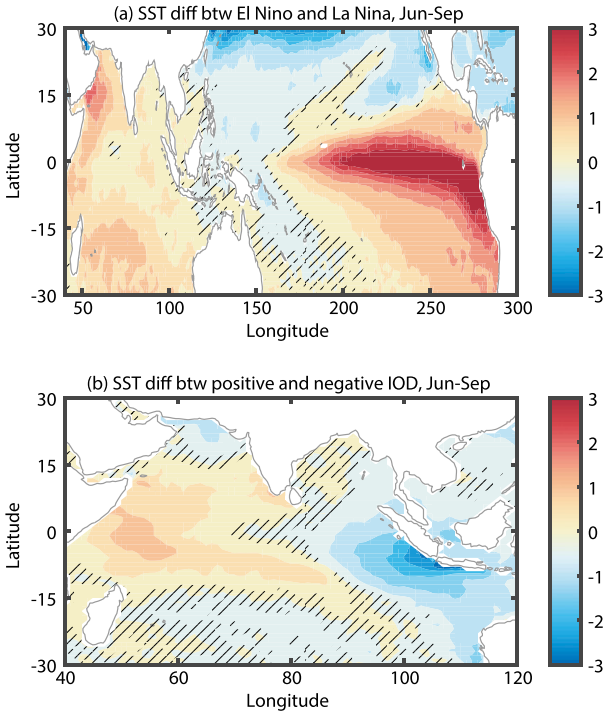

FIG. 10. SST differences (°C) during the Indian summer monsoon (from June to September) (a) between El Niño and La Niña and (b) between positive and negative IODZM phases. The differences in the hatched regions are not significant at a 95% confidence level.

during the Indian summer monsoon at interannual time scales.

Since ENSO and IODZM are two dominant interannual modes of variabilities over the Pacific and Indian Oceans, respectively, it is desirable to examine the influences of ENSO and IODZM on the interannual variability of the CIO mode. Note that we focus on the modulation of the CIO mode at interannual time scales and not on the interactions between ENSO and IODZM (Annamalai et al. 2003, 2005; Izumo et al. 2010). Since the CIO mode is active during the Indian summer monsoon but suppressed during boreal winter, we only focus on boreal summer in the following analysis. El Niño and La Niña are defined using the daily Niño-3.4 index (the daily mean SST over the Niño-3.4 region). The days during the Indian summer monsoon from 1982 to 2014 are categorized into two groups. The group that is composed of days with a Niño-3.4 index larger than the mean plus (minus) one standard deviation (STD) denotes the El Niño (La Niña) condition. Each group accounts for about 15% of total days during the Indian summer monsoon from 1982 to 2014. Goddard and Dilley (2005) and Camargo and Sobel (2005) used the upper 25% of total days for El Niño and lower 25% of total days for La Niña. Thus, the current criterion is stricter than the one they used. The difference of SST between El Niño and La Niña is shown in Fig. 10a. The warm anomalies from the central to the eastern Pacific Ocean are outstanding, and the El Niño and La Niña are clearly captured. The IODZM is identified with the daily dipole mode index (DMI) following Saji et al. (1999). By analogy to the criterion for El Niño and La Niña, the positive IODZM phase is defined when the DMI is larger than the mean plus one STD of the daily DMI during the Indian summer monsoon from 1982 to 2014, and the negative IODZM phase is defined when the DMI is smaller than the mean minus one STD. Figure 10b shows the SST difference between the positive and negative IODZM phases, and the IODZM pattern is also clearly reproduced. The SST differences between the IODZM phases and between the ENSO phases (Fig. 10) are quite different from the pattern of the CIO mode (Fig. 3a; Zhou et al. 2017). At the intraseasonal time scale, the CIO mode represents the ocean–atmosphere coupled features and the SST variation plays an important role in its evolution. In contrast, the low-frequency variabilities of the kinetic energy associated with the CIO mode are mainly due to the large-scale atmospheric circulation as shown above. Hence, the following analysis also focuses on the kinetic energy and the zonal wind structure in the atmosphere. However, this does not exclude the oceanic influences via other possible mechanisms, such as the oceanic impacts on the atmospheric boundary layer and the oceanic contribution to the accumulation of the available potential energy by modifying the surface heat flux.

The difference in $\partial\overline{u}/\partial y$ between the positive and negative IODZM phases is shown in Fig. 11. In deep tropics, the amplitudes of $\partial\overline{u}/\partial y$ are similar in the two phases, but there is a shift in the latitudinal location. In the northern Bay of Bengal around 20°N, $\partial\overline{u}/\partial y$ is much stronger in the negative IODZM than the positive IODZM. As a result, for the positive IODZM phase, $[\mathrm{KE}' \times \overline{\mathrm{KE}}]$ is smaller between 10°S and the equator but larger to the north between the equator and 10°N (Fig. 12). Over the northern Bay of Bengal also, $[\mathrm{KE}' \times \overline{\mathrm{KE}}]$ is smaller in the positive IODZM than the negative IODZM. The differences in precipitation are roughly consistent with $[\mathrm{KE}' \times \overline{\mathrm{KE}}]$ (Fig. 12d). Comparing the positive and negative IODZM phases, because of warm SST anomalies in the western Indian Ocean and the cold SST anomalies in the eastern Indian Ocean, easterly wind anomalies (denoted with δu) are generated (vectors in Fig. 13; Iizuka et al. 2000). Of course, the wind anomalies cannot be uniform in latitude. Hence, $d^2(\delta u)/dy^2$ is superimposed on the normal meridional gradient of relative vorticity. As shown in Fig. 13, the amplitude

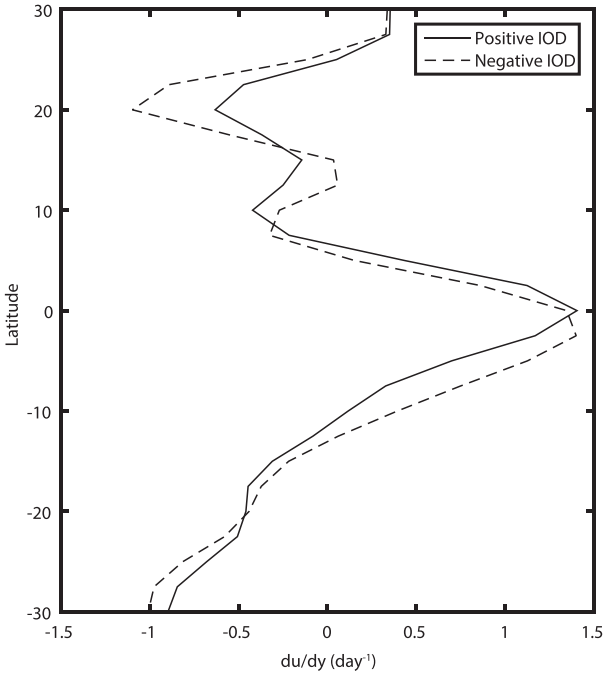

FIG. 11. Meridional gradient of zonal wind $\partial u/\partial y$ at 850 hPa, averaged between 80° and 90°E, during positive and negative IODZM phases.

of $d^2(\delta u)/dy^2$ is generally smaller than that of $\beta - \partial^2 U/\partial y^2$ shown in Fig. 5a. Thus, the modification of the differences between different IODZM phases only causes a moderate deviation from a normal year, which can also be confirmed from the pattern of $[KE' \times \overline{KE}]$ and precipitation in Fig. 12. Therefore, the IODZM phases do not change the amplitude of CIO mode significantly, but they shift the latitudes of the normal CIO mode slightly; that is, the positive (negative) IODZM tends to shift the CIO mode northward (southward) by a few degrees of latitude.

The difference in $\partial\overline{u}/\partial y$ over the central Indian Ocean between El Niño and La Niña is shown in Fig. 14. Generally, the differences between El Niño and La Niña are not large. But $\partial\overline{u}/\partial y$ is slightly stronger (for both positive and negative shears) during La Niña than it is during El Niño between 5°S and 10°N. Correspondingly, the barotropic energy conversion $[KE' \times \overline{KE}]$ and precipitation are slightly smaller during El Niño over the central Indian Ocean (Fig. 15). In addition, the wind difference at 850 hPa between El Niño and La Niña shows a cyclonic anomaly between 80° and 100°E along the equator, which is opposite to the anticyclonic cell for the CIO mode (Zhou et al. 2017). Thus, the CIO mode is expected to be slightly weaker during El Niño. Actually, pronounced differences between El Niño and La Niña reside in the western Pacific. Large differences in both $[KE' \times \overline{KE}]$ and precipitation extend in the southeast–northwest direction from the eastern tropical Pacific, going through the South China Sea (SCS) and reaching the Bay of Bengal. The southeast–northwest-tilting belt is continuous in the difference in $[KE' \times \overline{KE}]$ (color shading in Fig. 15, top) but seems to break down in the

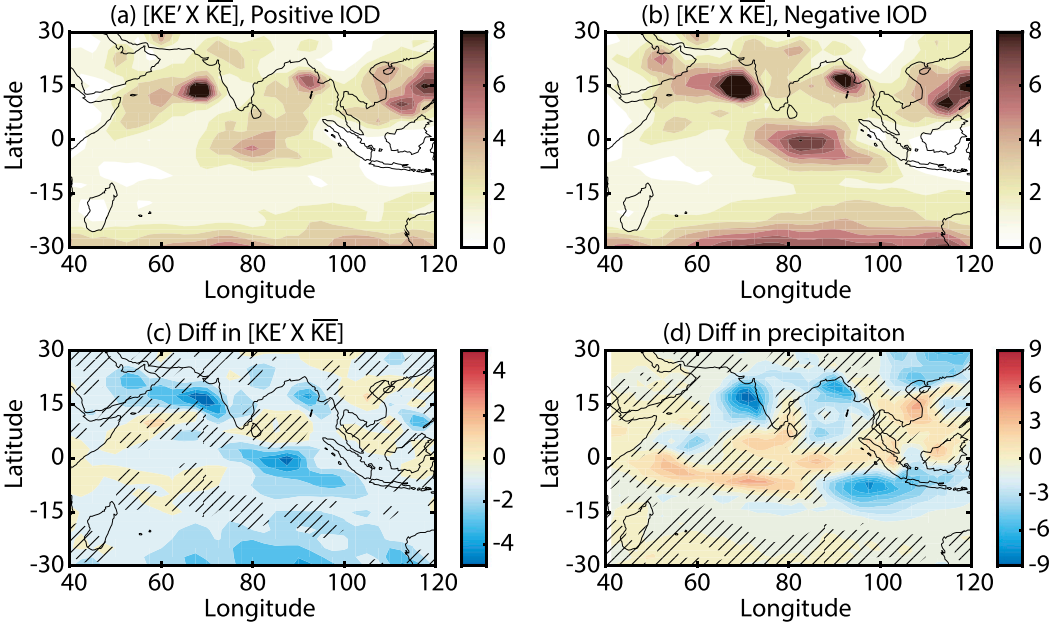

FIG. 12. Mean $[KE' \times \overline{KE}]$ at 850 hPa (J day^{-1} kg^{-1}) during (a) positive and (b) negative IODZM and (c) their differences. (d) Differences in precipitation between positive and negative IODZM phases (kg m^{-2} day^{-1}). The differences in the hatched regions are not significant at a 95% confidence level.

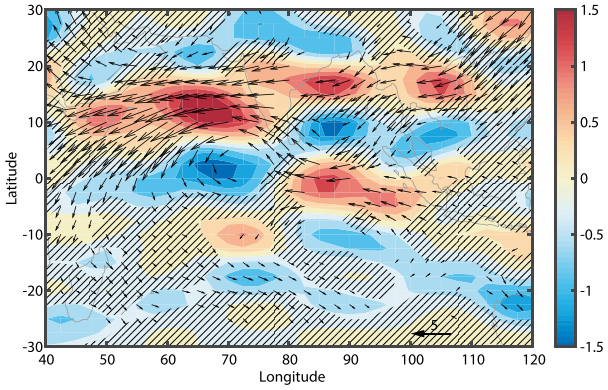

FIG. 13. Difference in winds $\delta\mathbf{u}$ at 850 hPa (vectors; m s^{-1}) and $d^2(\delta u)/dy^2$ (color shading; 10^{-11} m^{-1} s^{-1}) between the positive and the negative IODZM phases. The differences in the hatched regions are not significant at a 95% confidence level.

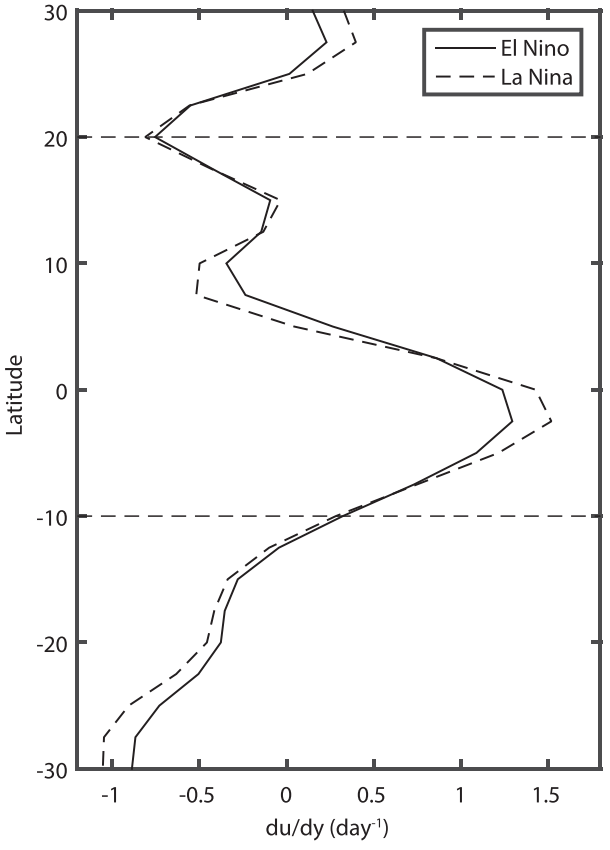

FIG. 14. Meridional gradient of zonal wind $\partial u/\partial y$ at 850 hPa, averaged between 80° and 90°E, during El Niño and La Niña.

difference in precipitation (color shading in Fig. 15, bottom), which is attributable to the small humidity difference between El Niño and La Niña over the Southeast Asian peninsula (not shown). Wang and Xie (1997) argued that the apparent northward propagation of intraseasonal variabilities was actually a westward-tilting convection front, which emanated from the tropical Pacific as Rossby waves. This hypothesis could not explain the independent northward-propagating intraseasonal variabilities as categorized in Wang and Rui (1990), and hence it may not be the whole story. However, it is supported by the evidence that many northward-propagating intraseasonal variabilities coincide with the westward-propagating ones, from observational evidence that many monsoon depressions and breaks are related to the variabilities coming from the east (Krishnan et al. 2000), and also from numerical model experiments of Annamalai et al. (2010). It is now also supported by the southeast–northwest-tilting belt of $[\mathrm{KE}' \times \overline{\mathrm{KE}}]$ and precipitation shown in Fig. 15. Therefore, it can be concluded that there is more than one avenue for ENSO to influence the Indian Ocean in reality. The westward-propagating Rossby waves are likely to be an important pathway and the ENSO influence via modifying the CIO mode is another avenue. Actually, ENSO can also have impacts on the Indian Ocean via the Indonesian Throughflow (ITF; e.g., Murtugudde et al. 1998; Reason et al. 2000; Lee et al. 2002; Zhou et al. 2008b,a; and many others) and by altering the temperature difference between SST and the tropospheric temperature as well (Chiang and Sobel 2002). The complex and multichannel connections between ENSO and the Indian Ocean may explain the weak linear correlation between ENSO and the Indian summer monsoon. A better understanding of the net effect of these various avenues and their relative importance for different ENSO events can be expected to benefit the simulation and prediction of Indian summer monsoon. We also expect that employing the Indo-Pacific tripole framework (Chen 2011) and diagnosing each term in Eq. (4) for their interannual variability may shed more light on the apparent nonstationarity of the ENSO–IODZM–monsoon interactions. But this is beyond the scope of this study.

5. Conclusions and discussion

The CIO mode is found to be closely related to the MISO and heavy monsoonal rainfall during the Indian summer monsoon. The processes associated with the CIO mode at intraseasonal time scales have been discussed in Zhou et al. (2017). In addition to the intraseasonal variabilities, the CIO mode also has pronounced seasonal and interannual variabilities. The low-frequency variabilities of the CIO mode are attributable to barotropic instability, which is triggered when the meridional shear of the background zonal winds are large enough to overcome the meridional

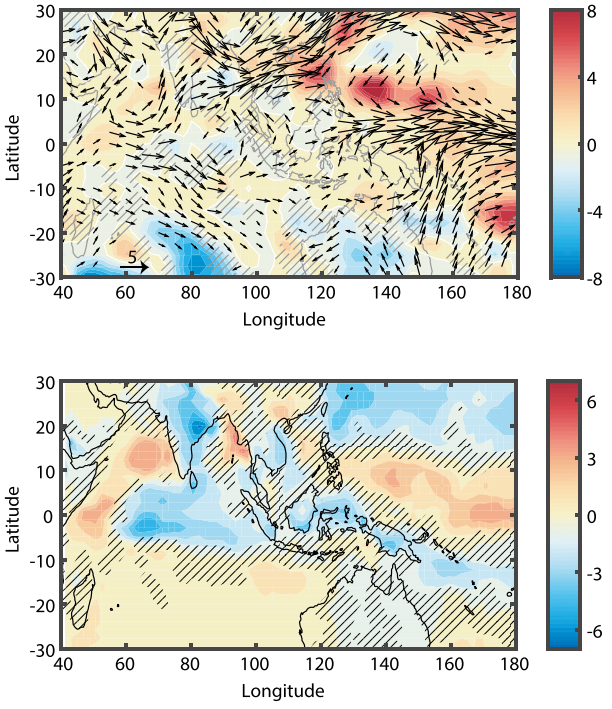

FIG. 15. (top) Difference in $[KE' \times \overline{KE}]$ at 850 hPa (color shading; J day^{-1} kg^{-1}) and in winds at 850 hPa (vectors; m s^{-1}) between El Niño and La Niña during the Indian summer monsoon (from June to September). (bottom) Difference in precipitation between El Niño and La Niña (kg m^{-2} day^{-1}). The differences in the hatched regions are not significant at a 95% confidence level.

gradient of the planetary vorticity. The energy conversion from zonal mean kinetic energy to the kinetic energy of intraseasonal variabilities energizes the intraseasonal variabilities during the Indian summer monsoon and leads to an active CIO mode. The horizontal eddy flux is the major component for the variation of the meridional gradient of zonal winds, which is consistent with the traditional conclusion for the global mean zonal velocity as discussed in Holton and Hakim (2013), albeit mostly in the context of midlatitude circulation. At interannual time scales, ENSO and IODZM are two dominant modes over the Indo-Pacific region. IODZM tends to shift the latitudinal position of the CIO mode by modifying the meridional shear of the zonal winds, since large-scale zonal winds are induced by the SST anomalies in the western and eastern nodes of IODZM. ENSO has moderate impacts on the interannual variability of the CIO mode; El Niño tends to weaken the CIO mode and La Niña tends to enhance it, via the changes in the low-level zonal wind shear over the central Indian Ocean. Overall, the impacts of ENSO and IODZM on the CIO mode at the interannual time scale are both moderate, which is consistent with the fact that the relations between ENSO/IODZM and Indian summer monsoon are weak and unreliable (e.g., Kumar et al. 1999; Krishnamurthy and Kirtman 2003). The weak statistical correlation between ENSO/IODZM and Indian summer monsoon was also shown in Zhou et al. (2017). At the intraseasonal time scale, Zhou et al. (2017) showed that the CIO mode represents a mechanistic link between the CIO mode and the Indian summer monsoon; that is, the CIO mode has an impact on the MISO via creating a coherent environment between the SST anomalies and the cyclonic gyre over the central Indian Ocean and modifying the vertical structure of the wind field. In this study, we conclude that the seasonal and the interannual variabilities of the CIO mode are also consistent with those of the Indian summer monsoon.

The seasonal variability of the CIO mode is quite consistent with that of the Indian monsoon. It represents the seasonal shift of the ITCZ and precipitation between the Northern and Southern Hemispheres. The observations and reanalysis products for SST and low-level winds (e.g., at 850 hPa) are fairly reliable. The simulation and prediction of these large-scale variables are also satisfactory. Thus, a better understanding of the relation between the CIO mode and the Indian summer monsoon is likely to facilitate the simulation and prediction of the intraseasonal features of the Indian monsoon and their low-frequency variabilities, especially the monsoon onset and withdrawal. At interannual and longer time scales, the evolution of the Indian monsoon system follows the shift of the ITCZ between the two hemispheres as well. The global energy balance determines the ITCZ locations at interannual and longer time scales (Schneider et al. 2014). Zhou et al. (2017) showed that the CIO mode, which captures the atmosphere–ocean interactions at the intraseasonal time scale, plays an important role in the MISO phenomenon. Current results show that the barotropic energy conversion resulting from the large-scale wind structures is undoubtedly a key process in the energy budget over the Indian Ocean during the Indian summer monsoon. In the multiscale but "seamless" climate system, the CIO mode is certainly influenced by the background state variability, such as ENSO and IODZM, as discussed in this study. On the other hand, it is also foreseen that the CIO mode may have feedbacks to the background state, which requires further studies in the future.

A caveat of this study is that the potential energy budget associated with the low-frequency variabilities of the CIO mode is not shown because of the uncertainty of key variables in the reanalysis products. The latent heat release and the moist processes are critical for the variation of the potential energy. But large uncertainty

exists not only in reanalysis products but also in observations. For example, Zhang et al. (2010) showed inconsistency in shallow diabatic heating between four different Tropical Rainfall Measuring Mission (TRMM) datasets. Therefore, it is hard to yield reliable estimates of the potential energy budget using existing observations or reanalysis products. An idealized layer model (which has been widely used in theoretical studies, such as in Moorthi and Arakawa 1985; Chatterjee and Goswami 2004; Sobel and Maloney 2012; Liu and Wang 2013; Zhou and Kang 2013; and many others) should be a useful tool for detecting the influences of moist processes on the CIO mode at various time scales. It can also be useful for further examining the mechanisms of the CIO mode and the sensitivity of the CIO mode to the parameterization of moist processes. In all, much more work is needed for a better understanding of the CIO mode and its relation with the Indian monsoon in the multiscale climate system.

Acknowledgments. This work is supported by grants from the National Natural Science Foundation of China (41376034, 41321004, 41690121, and 41690120), the National Basic Research Program (2013CB430302), and the IPOVAR Project (GASI-IPOVAI-01-02 and GASI-IPOVAI-02). RM gratefully acknowledges the CYGNSS grant from NASA and the National Monsoon Mission funds for partial support. We deeply appreciate the comments from the editor and the reviewers on all aspects of our analysis, which helped sharpen our message.

APPENDIX

Derivations of the Zonal Momentum Equation

The derivation of the zonal mean zonal velocity equation is similar to the one presented in Holton and Hakim (2013), except that the advection and vertical eddy flux, which were neglected in their study, are retained in this study. In addition, since the zonal mean is taken within a bounded region (such as the Indian Ocean) rather than over the whole globe, the influences from the western and the eastern boundaries are considered.

The zonal momentum equation in isobaric coordinates is

$$\frac{Du}{Dt} - (f+\beta y)v + \frac{\partial \Phi}{\partial x} = X, \tag{A1}$$

where u and v are the zonal and meridional velocities, f is the Coriolis parameter, $\beta = df/dy$, Φ is the geopotential, X is the residual term, and $D/Dt = \partial/\partial t + u\partial/\partial x + v\partial/\partial y + \omega\partial/\partial p$. Using the continuity equation $\partial u/\partial x + \partial v/\partial y + \partial\omega/\partial p = 0$, the flux form of the material derivative of u is

$$\frac{Du}{Dt} = \frac{\partial u}{\partial t} + \frac{\partial u^2}{\partial x} + \frac{\partial uv}{\partial y} + \frac{\partial u\omega}{\partial p}. \tag{A2}$$

Taking the zonal average within a domain $\overline{(\cdot)} = L^{-1}\int_W^E dx$, where L is the zonal length of the region, W denotes the western boundary, and E denotes the eastern boundary), one has

$$\frac{\overline{Du}}{Dt} = \frac{\partial \overline{u}}{\partial t} + \overline{\frac{\partial u^2}{\partial x}} + \frac{\partial \overline{uv}}{\partial y} + \frac{\partial \overline{u\omega}}{\partial p}. \tag{A3}$$

All variables in Eq. (A3) are written as the zonal mean within the region (rather than the global zonal mean) and the deviation from the zonal mean (i.e., $u = \overline{u} + u'$). Then, one has $\overline{u'} = 0$, $\overline{uv} = \overline{u}\,\overline{v} + \overline{u'v'}$, and $\overline{\partial u^2/\partial x} = L^{-1}(u^2|_E - u^2|_W) \equiv L^{-1}\Delta(u^2)$, where Δ denotes the difference between the values at the eastern and the western boundaries. Thus, Eq. (A3) becomes

$$\frac{\overline{Du}}{Dt} = \frac{\partial \overline{u}}{\partial t} + \frac{\Delta(u^2)}{L} + \frac{\partial}{\partial y}(\overline{u}\,\overline{v} + \overline{u'v'}) + \frac{\partial}{\partial p}(\overline{u}\,\overline{\omega} + \overline{u'\omega'}). \tag{A4}$$

The regional zonal mean of the continuity equation yields

$$\frac{\partial \overline{v}}{\partial y} + \frac{\partial \overline{\omega}}{\partial p} = -\frac{\Delta u'}{L}. \tag{A5}$$

Plugging Eq. (A5) into Eq. (A4), one has

$$\frac{\overline{Du}}{Dt} = \frac{\overline{D}}{Dt}\overline{u} + \frac{\partial \overline{u'v'}}{\partial y} + \frac{\partial \overline{u'\omega'}}{\partial p} + \frac{\overline{u}\Delta u' + \Delta(u'u')}{L}, \tag{A6}$$

where $\overline{D}/Dt = \partial/\partial t + \overline{v}\partial/\partial y + \overline{\omega}\partial/\partial p$.

Using Eq. (A6), the zonal mean of Eq. (A1) within a domain is written as

$$\frac{\overline{D}}{Dt}\overline{u} + \frac{\partial \overline{u'v'}}{\partial y} + \frac{\partial \overline{u'\omega'}}{\partial p} + \frac{\overline{u}\Delta u' + \Delta(u'u')}{L} - (f+\beta y)\overline{v} + \overline{\frac{\partial \Phi}{\partial x}} = \overline{X}. \tag{A7}$$

Thus, the zonal mean tendency of zonal velocity becomes

$$\frac{\partial \overline{u}}{\partial t} = -\left(\overline{v}\frac{\partial}{\partial y} + \overline{\omega}\frac{\partial}{\partial p}\right)\overline{u} - (f+\beta y)\overline{v} - \frac{\partial}{\partial y}(\overline{u'v'}) - \frac{\partial}{\partial p}(\overline{u'\omega'}) - \frac{\overline{u}\Delta u' + \Delta(u'u') + \Delta\Phi'}{L} + \overline{X}, \tag{A8}$$

which is Eq. (3) in the main text. Taking the y derivative of Eq. (A8), one has

$$\frac{\partial}{\partial t}\left(\frac{\partial \overline{u}}{\partial y}\right) = -\frac{\partial \overline{v}}{\partial y}\frac{\partial \overline{u}}{\partial y} - \overline{v}\frac{\partial^2 \overline{u}}{\partial y^2} - \frac{\partial \overline{\omega}}{\partial y}\frac{\partial \overline{u}}{\partial p} - \overline{\omega}\frac{\partial^2 \overline{u}}{\partial y \partial p} - (f+\beta y)\frac{\partial \overline{v}}{\partial y} - \beta \overline{v} - \frac{\partial^2 \overline{u'v'}}{\partial y^2} - \frac{\partial^2 \overline{u'\omega'}}{\partial y \partial p} - \frac{\partial}{\partial y}\left[\frac{\Delta(uu' + \Phi')}{L}\right] + \frac{\partial \overline{X}}{\partial y}, \quad \text{(A9)}$$

which is Eq. (4) in the main text.

REFERENCES

Annamalai, H., and M. J. Slingo, 2001: Active/break cycles: Diagnosis of the intraseasonal variability of the Asian summer monsoon. *Climate Dyn.*, **18**, 85–102, doi:10.1007/s003820100161.

——, R. Murtugudde, J. Potemra, S. P. Xie, P. Liu, and B. Wang, 2003: Coupled dynamics over the Indian Ocean: Spring initiation of the zonal mode. *Deep-Sea Res. II*, **50**, 2305–2330, doi:10.1016/S0967-0645(03)00058-4.

——, S. P. Xie, J. P. McCreary, and R. Murtugudde, 2005: Impact of Indian Ocean sea surface temperature on developing El Niño. *J. Climate*, **18**, 302–319, doi:10.1175/JCLI-3268.1.

——, S. Kida, and J. Hafner, 2010: Potential impact of the tropical Indian Ocean–Indonesian Seas on El Niño characteristics. *J. Climate*, **23**, 3933–3952, doi:10.1175/2010JCLI3396.1.

Ashok, K., Z. Guan, and T. Yamagata, 2001: Impact of the Indian Ocean dipole on the relationship between the Indian monsoon rainfall and ENSO. *Geophys. Res. Lett.*, **28**, 4499–4502, doi:10.1029/2001GL013294.

——, ——, N. H. Saji, and T. Yamagata, 2004: Individual and combined influences of ENSO and the Indian Ocean dipole on the Indian summer monsoon. *J. Climate*, **17**, 3141–3155, doi:10.1175/1520-0442(2004)017<3141:IACIOE>2.0.CO;2.

Bordoni, S., and T. Schneider, 2008: Monsoons as eddy-mediated regime transitions of the tropical overturning circulation. *Nat. Geosci.*, **1**, 515–519, doi:10.1038/ngeo248.

Bretherton, C. S., M. Widmann, V. P. Dymnikov, J. M. Wallace, and I. Bladé, 1999: The effective number of spatial degrees of freedom of a time-varying field. *J. Climate*, **12**, 1990–2009, doi:10.1175/1520-0442(1999)012<1990:TENOSD>2.0.CO;2.

Camargo, S. J., and A. H. Sobel, 2005: Western North Pacific tropical cyclone intensity and ENSO. *J. Climate*, **18**, 2996–3006, doi:10.1175/JCLI3457.1.

Charney, J. G., and M. E. Stern, 1962: On the stability of internal baroclinic jets in a rotating atmosphere. *J. Atmos. Sci.*, **19**, 159–172, doi:10.1175/1520-0469(1962)019<0159:OTSOIB>2.0.CO;2.

Chatterjee, P., and B. N. Goswami, 2004: Structure, genesis and scale selection of the tropical quasi-biweekly mode. *Quart. J. Roy. Meteor. Soc.*, **130**, 1171–1194, doi:10.1256/qj.03.133.

Chen, D., 2011: Indo-Pacific tripole: An intrinsic mode of tropical climate variability. *Advances in Geosciences*, J. Gan, Ed., World Scientific, 1–18.

Chiang, J. C. H., and A. H. Sobel, 2002: Tropical tropospheric temperature variations caused by ENSO and their influence on the remote tropical climate. *J. Climate*, **15**, 2616–2631, doi:10.1175/1520-0442(2002)015<2616:TTTVCB>2.0.CO;2.

Fasullo, J., and P. J. Webster, 2003: A hydrological definition of Indian monsoon onset and withdrawal. *J. Climate*, **16**, 3200–3211, doi:10.1175/1520-0442(2003)016<3200a:AHDOIM>2.0.CO;2.

Fu, X. H., and B. Wang, 2004: Differences of boreal summer intraseasonal oscillations simulated in an atmosphere–ocean coupled model and an atmosphere-only model. *J. Climate*, **17**, 1263–1271, doi:10.1175/1520-0442(2004)017<1263:DOBSIO>2.0.CO;2.

Gadgil, S., P. N. Vinayachandran, P. A. Francis, and S. Gadgil, 2004: Extremes of the Indian summer monsoon rainfall, ENSO and equatorial Indian Ocean oscillation. *Geophys. Res. Lett.*, **31**, L12213, doi:10.1029/2004GL019733.

Goddard, L., and M. Dilley, 2005: El Niño: Catastrophe or opportunity. *J. Climate*, **18**, 651–665, doi:10.1175/JCLI-3277.1.

Goswami, B. N., 2005: South Asian monsoon. *Intraseasonal Variability in the Atmosphere-Ocean Climate System*, W. Lau and D. Waliser, Eds., Springer, 19–61.

——, and P. K. Xavier, 2005: ENSO control on the south Asian monsoon through the length of the rainy season. *Geophys. Res. Lett.*, **32**, L18717, doi:10.1029/2005GL023216.

Holton, J. R., and G. J. Hakim, 2013: The general circulation. *An Introduction to Dynamic Meteorology*, 5th ed. J. R. Holton and G. J. Hakim, Eds., Academic Press, 325–375.

Iizuka, S., T. Matsuura, and T. Yamagata, 2000: The Indian Ocean SST dipole simulated in a coupled general circulation model. *Geophys. Res. Lett.*, **27**, 3369–3372, doi:10.1029/2000GL011484.

Izumo, T., and Coauthors, 2010: Influence of the state of the Indian Ocean dipole on the following year's El Niño. *Nat. Geosci.*, **3**, 168–172, doi:10.1038/ngeo760.

Jiang, X. N., T. Li, and B. Wang, 2004: Structures and mechanisms of the northward propagating boreal summer intraseasonal oscillation. *J. Climate*, **17**, 1022–1039, doi:10.1175/1520-0442(2004)017<1022:SAMOTN>2.0.CO;2.

Kalnay, E., and Coauthors, 1996: The NCEP/NCAR 40-Year Reanalysis Project. *Bull. Amer. Meteor. Soc.*, **77**, 437–471, doi:10.1175/1520-0477(1996)077<0437:TNYRP>2.0.CO;2.

Kang, I.-S., D. Kim, and J.-S. Kug, 2010: Mechanism for northward propagation of boreal summer intraseasonal oscillation: Convective momentum transport. *Geophys. Res. Lett.*, **37**, L24804, doi:10.1029/2010GL045072.

Karmakar, N., A. Chakraborty, and R. S. Nanjundiah, 2015: Decreasing intensity of monsoon low-frequency intraseasonal variability over India. *Environ. Res. Lett.*, **10**, 054018, doi:10.1088/1748-9326/10/5/054018.

Kemball-Cook, S., and B. Wang, 2001: Equatorial waves and air–sea interaction in the boreal summer intraseasonal oscillation. *J. Climate*, **14**, 2923–2942, doi:10.1175/1520-0442(2001)014<2923:EWAASI>2.0.CO;2.

Krishnamurthy, V., and B. N. Goswami, 2000: Indian monsoon–ENSO relationship on interdecadal timescale. *J. Climate*, **13**, 579–595, doi:10.1175/1520-0442(2000)013<0579:IMEROI>2.0.CO;2.

——, and B. P. Kirtman, 2003: Variability of the Indian Ocean: Relation to monsoon and ENSO. *Quart. J. Roy. Meteor. Soc.*, **129**, 1623–1646, doi:10.1256/qj.01.166.

Krishnan, R., C. Zhang, and M. Sugi, 2000: Dynamics of breaks in the Indian summer monsoon. *J. Atmos. Sci.*, **57**, 1354–1372, doi:10.1175/1520-0469(2000)057<1354:DOBITI>2.0.CO;2.

Kumar, K. K., B. Rajagopalan, and M. A. Cane, 1999: On the weakening relationship between the Indian monsoon

and ENSO. *Science*, **284**, 2156–2159, doi:10.1126/science.284.5423.2156.

Lau, N.-C., and M. J. Nath, 2004: Coupled GCM simulation of atmosphere–ocean variability associated with zonally asymmetric SST changes in the tropical Indian Ocean. *J. Climate*, **17**, 245–265, doi:10.1175/1520-0442(2004)017<0245:CGSOAV>2.0.CO;2.

Lee, T., I. Fukumori, D. Menemenlis, Z. Xing, and L.-L. Fu, 2002: Effects of the Indonesian Throughflow on the Pacific and Indian Oceans. *J. Phys. Oceanogr.*, **32**, 1404–1429, doi:10.1175/1520-0485(2002)032<1404:EOTITO>2.0.CO;2.

Li, T., B. Wang, C. P. Chang, and Y. Zhang, 2003: A theory for the Indian Ocean dipole–zonal mode. *J. Atmos. Sci.*, **60**, 2119–2135, doi:10.1175/1520-0469(2003)060<2119:ATFTIO>2.0.CO;2.

Lian, T., D. Chen, Y. Tang, and Q. Wu, 2014: Effects of westerly wind bursts on El Niño: A new perspective. *Geophys. Res. Lett.*, **41**, 3522–3527, doi:10.1002/2014GL059989.

Liebmann, B., and C. A. Smith, 1996: Description of a complete (interpolated) outgoing longwave radiation dataset. *Bull. Amer. Meteor. Soc.*, **77**, 1275–1277.

Liu, F., and B. Wang, 2013: An air–sea coupled skeleton model for the Madden–Julian oscillation. *J. Atmos. Sci.*, **70**, 3147–3156, doi:10.1175/JAS-D-12-0348.1.

Longuet-Higgins, M. S., 1984: Statistical properties of wave groups in a random sea state. *Philos. Trans. Roy. Soc. London*, **312A**, 219–250, doi:10.1098/rsta.1984.0061.

Moorthi, S., and A. Arakawa, 1985: Baroclinic instability with cumulus heating. *J. Atmos. Sci.*, **42**, 2007–2031, doi:10.1175/1520-0469(1985)042<2007:BIWCH>2.0.CO;2.

Murtugudde, R., A. J. Busalacchi, and J. Beauchamp, 1998: Seasonal-to-interannual effects of the Indonesian Throughflow on the tropical Indo-Pacific basin. *J. Geophys. Res.*, **103**, 21 425–21 441, doi:10.1029/98JC02063.

Ouergli, A., 2002: Hilbert transform from wavelet analysis to extract the envelope of an atmospheric mode: Examples. *J. Atmos. Oceanic Technol.*, **19**, 1082–1086, doi:10.1175/1520-0426(2002)019<1082:HTFWAT>2.0.CO;2.

Pottapinjara, V., M. S. Girishkumar, M. Ravichandran, and R. Murtugudde, 2014: Influence of the Atlantic zonal mode on monsoon depressions in the Bay of Bengal during boreal summer. *J. Geophys. Res. Atmos.*, **119**, 6456–6469, doi:10.1002/2014JD021494.

——, ——, S. Sivareddy, M. Ravichandran, and R. Murtugudde, 2016: Relation between the upper ocean heat content in the equatorial Atlantic during boreal spring and the Indian monsoon rainfall during June–September. *Int. J. Climatol.*, **36**, 2469–2480, doi:10.1002/joc.4506.

Rajeevan, M., S. Gadgil, and J. Bhate, 2010: Active and break spells of the Indian summer monsoon. *J. Earth Syst. Sci.*, **119**, 229–247, doi:10.1007/s12040-010-0019-4.

Reason, C. J. C., R. J. Allan, J. A. Lindesay, and T. J. Ansell, 2000: ENSO and climatic signals across the Indian Ocean Basin in the global context: Part I, interannual composite patterns. *Int. J. Climatol.*, **20**, 1285–1327, doi:10.1002/1097-0088(200009)20:11<1285::AID-JOC536>3.0.CO;2-R.

Reynolds, R. W., T. M. Smith, C. Liu, D. B. Chelton, K. S. Casey, and M. G. Schlax, 2007: Daily high-resolution-blended analyses for sea surface temperature. *J. Climate*, **20**, 5473–5496, doi:10.1175/2007JCLI1824.1.

Roxy, M. K., K. Ritika, P. Terray, R. Murtugudde, K. Ashok, and B. N. Goswami, 2015: Drying of Indian subcontinent by rapid Indian Ocean warming and a weakening land-sea thermal gradient. *Nat. Commun.*, **6**, 7423, doi:10.1038/ncomms8423.

Sabeerali, C. T., S. A. Rao, G. George, D. N. Rao, S. Mahapatra, A. Kulkarni, and R. Murtugudde, 2014: Modulation of monsoon intraseasonal oscillations in the recent warming period. *J. Geophys. Res. Atmos.*, **119**, 5185–5203, doi:10.1002/2013JD021261.

——, ——, A. R. Dhakate, K. Salunke, and B. N. Goswami, 2015: Why ensemble mean projection of South Asian monsoon rainfall by CMIP5 models is not reliable? *Climate Dyn.*, **45**, 161–174, doi:10.1007/s00382-014-2269-3.

Saha, A., S. Ghosh, A. S. Sahana, and E. P. Rao, 2014: Failure of CMIP5 climate models in simulating post-1950 decreasing trend of Indian monsoon. *Geophys. Res. Lett.*, **41**, 7323–7330, doi:10.1002/2014GL061573.

Sahana, A. S., G. Subimal, G. Auroop, and M. Raghu, 2015: Shift in Indian summer monsoon onset during 1976/1977. *Environ. Res. Lett.*, **10**, 054006, doi:10.1088/1748-9326/10/5/054006.

Saji, N. H., B. N. Goswami, P. N. Vinayachandran, and T. Yamagata, 1999: A dipole mode in the tropical Indian Ocean. *Nature*, **401**, 360–363.

Sarkar, S., R. P. Singh, and M. Kafatos, 2004: Further evidences for the weakening relationship of Indian rainfall and ENSO over India. *Geophys. Res. Lett.*, **31**, L13209, doi:10.1029/2004GL020259.

Schneider, T., T. Bischoff, and G. H. Haug, 2014: Migrations and dynamics of the intertropical convergence zone. *Nature*, **513**, 45–53, doi:10.1038/nature13636.

Shukla, R. P., 2014: The dominant intraseasonal mode of intraseasonal South Asian summer monsoon. *J. Geophys. Res. Atmos.*, **119**, 635–651, doi:10.1002/2013JD020335.

Slingo, J. M., and H. Annamalai, 2000: 1997: The El Niño of the century and the response of the Indian summer monsoon. *Mon. Wea. Rev.*, **128**, 1778–1797, doi:10.1175/1520-0493(2000)128<1778:TENOOT>2.0.CO;2.

Sobel, A., and E. Maloney, 2012: An idealized semi-empirical framework for modeling the Madden–Julian oscillation. *J. Atmos. Sci.*, **69**, 1691–1705, doi:10.1175/JAS-D-11-0118.1.

Uppala, S. M., and Coauthors, 2005: The ERA-40 Re-Analysis. *Quart. J. Roy. Meteor. Soc.*, **131**, 2961–3012, doi:10.1256/qj.04.176.

Vallis, G. K., 2006: *Atmospheric and Oceanic Fluid Dynamics.* Cambridge University Press, 745 pp.

Waliser, D. E., 2006: Intraseasonal variability. *The Asian Monsoon*, B. Wang, Ed., Springer, 203–257.

Wang, B., and H. Rui, 1990: Synoptic climatology of transient tropical intraseasonal convection anomalies: 1975–1985. *Meteor. Atmos. Phys.*, **44**, 43–61, doi:10.1007/BF01026810.

——, and X. Xie, 1997: A model for the boreal summer intraseasonal oscillation. *J. Atmos. Sci.*, **54**, 72–86, doi:10.1175/1520-0469(1997)054<0072:AMFTBS>2.0.CO;2.

Webster, P. J., 1983: Mechanisms of monsoon low-frequency variability: Surface hydrological effects. *J. Atmos. Sci.*, **40**, 2110–2124, doi:10.1175/1520-0469(1983)040<2110:MOMLFV>2.0.CO;2.

——, and T. N. Palmer, 1997: The past and the future of El Niño. *Nature*, **390**, 562–564, doi:10.1038/37499.

Wu, G., and Y. Zhang, 1998: Tibetan Plateau forcing and the timing of the monsoon onset over South Asia and the South China Sea. *Mon. Wea. Rev.*, **126**, 913–927, doi:10.1175/1520-0493(1998)126<0913:TPFATT>2.0.CO;2.

Xi, J., L. Zhou, R. Murtugudde, and L. Jiang, 2015: Impacts of intraseasonal SST anomalies on precipitation during Indian summer monsoon. *J. Climate*, **28**, 4561–4575, doi:10.1175/JCLI-D-14-00096.1.

Yano, J.-I., and J. L. McBride, 1998: An aquaplanet monsoon. *J. Atmos. Sci.*, **55**, 1373–1399, doi:10.1175/1520-0469(1998)055<1373:AAM>2.0.CO;2.

Yasunari, T., 1980: A quasi-stationary appearance of 30 to 40 day period in the cloudiness fluctuations during the summer monsoon over India. *J. Meteor. Soc. Japan*, **58**, 225–229.

Zhang, C., and Coauthors, 2010: MJO signals in latent heating: Results from TRMM retrievals. *J. Atmos. Sci.*, **67**, 3488–3508, doi:10.1175/2010JAS3398.1.

Zhou, L., and I.-S. Kang, 2013: Influence of convective momentum transport on mixed Rossby–gravity waves: A contribution to tropical 2-day waves. *J. Atmos. Sci.*, **70**, 2467–2475, doi:10.1175/JAS-D-12-0300.1.

——, and R. Murtugudde, 2014: Impact of northward-propagating intraseasonal variability on the onset of Indian summer monsoon. *J. Climate*, **27**, 126–139, doi:10.1175/JCLI-D-13-00214.1.

——, ——, and M. Jochum, 2008a: Dynamics of the intraseasonal oscillations in the Indian Ocean South Equatorial Current. *J. Phys. Oceanogr.*, **38**, 121–132, doi:10.1175/2007JPO3730.1.

——, ——, and ——, 2008b: Seasonal influence of Indonesian Throughflow in the southwestern Indian Ocean. *J. Phys. Oceanogr.*, **38**, 1529–1541, doi:10.1175/2007JPO3851.1.

——, A. H. Sobel, and R. Murtugudde, 2012: Kinetic energy budget for the Madden–Julian oscillation in a multiscale framework. *J. Climate*, **25**, 5386–5403, doi:10.1175/JCLI-D-11-00339.1.

——, R. Murtugudde, D. Chen, and Y. Tang, 2017: A central Indian Ocean mode and heavy precipitation during the Indian summer monsoon. *J. Climate*, **30**, 2055–2067, doi:10.1175/JCLI-D-16-0347.1.